## Towards sustainable transparent flexible heaters: integration of a BNNT interlayer using green solvent substitution

Wagner, Kaitlin; Zou, Shan; Martinez-Rubi, Yadienka; Kell, Arnold J.; Paquet, Chantal; Lessard, Benoît H.



**Publisher's version / Version de l'éditeur:**
https://doi.org/10.1088/2058-8585/acc9d2
*Flexible and Printed Electronics, 8, 2, pp. 1-10, 2023-04-25*

Flexible and Printed Electronics

PAPER

# Towards sustainable transparent flexible heaters: Integration of a BNNT interlayer using green solvent substitution

**Kaitlin Wagner**[1,2], **Shan Zou**[3], **Yadienka Martinez-Rubi**[2], **Arnold J Kell**[2,*], **Chantal Paquet**[2] **and Benoît H Lessard**[1,4,*]

[1] University of Ottawa, Department of Chemical and Biological Engineering, 161 Louis Pasteur, Ottawa, ON K1N 6N5, Canada
[2] Security and Disruptive Technologies, National Research Council Canada, 100 Sussex Drive, Ottawa, ON K1A 0R6, Canada
[3] Metrology Research Centre, National Research Council Canada, 100 Sussex Drive, Ottawa, ON K1A 0R6, Canada
[4] School of Electrical Engineering and Computer Science, University of Ottawa, 800 King Edward Ave, Ottawa, Ontario K1N 6N5, Canada
[*] Authors to whom any correspondence should be addressed.

**E-mail:** Arnold.Kell@nrc-cnrc.gc.ca and benoit.lessard@uottawa.ca

**Keywords:** sustainability, green solvent, boron nitride nanotubes, polyvinyl butyral, printed electronics, transparent heater, interlayer

Supplementary material for this article is available online

OPEN ACCESS

RECEIVED
13 December 2022

REVISED
17 March 2023

ACCEPTED FOR PUBLICATION
3 April 2023

PUBLISHED
25 April 2023



## Abstract

Processing materials in electronics with non-toxic, green solvents can provide environmental benefits while reducing manufacturing health and safety challenges. Unfortunately, green solvents are often unable to provide comparable solubilizing characteristics and present challenges in printing and film formation compared to conventional organic solvents. Therefore, green materials are often developed in parallel to their processing method for successful implementation. In this study, we report on the use of a polyvinyl butyral (PVB) and ethanol solution as a replacement for poly (3-hexylthiophene-2,5-diyl) (P3HT) and chloroform and its' first demonstration in boron nitride nanotube (BNNT) thin film interlayers for improved thermal and mechanical performance in silver microgrid transparent heaters. Using PVB/ethanol led to comparable thin films of BNNT, achieving a clear tube network formation across the substrate surface and resulting in near identical optical transparency and surface energy measurements compared to the P3HT/chloroform system. Silver microgrids printed on BNNT-coated polyethylene terephthalate (PET) with PVB as dispersant exhibited a similar conductive performance to the microgrids printed on BNNT-coated PET with P3HT, providing the same level of mechanical endurance and maintaining thermal performance metrics upon applied voltage. The PVB and ethanol system presents an exemplary green material combination for the novel deposition of BNNT thin film interlayers for integration into transparent heaters.

## 1. Introduction

Printed electronics represents a growing field with enormous potential for providing low-cost sensors [1–4], smart label packaging [5], circuitry [6, 7] and more. Typically, the active coatings in these applications are printed using toxic or carcinogenic organic solvents [8]. As the large-scale deployment of printed electronics becomes a reality, environmental consequences over the use of these solvents increase in addition to growing concern towards the safety of printer operators. The choice of green solvents is limited, and often their chemical properties, such as vapor pressure, viscosity, and boiling point are different than existing organic solvents, making a simple change in solution rare [9–14]. The emphasis on sustainable electronics practices has transitioned to include device interlayers, which are useful in a variety of capacities including improving substrate roughness, printability, and ink adhesion for printed electronic devices [15–17]. Research on incorporating 'green' solvents without compromising the integrity of the material or the device's performance metrics is paramount for the integration of sustainable architectures.

Printed transparent heaters is an emerging electronic application that has found functions in automotive, aerospace and medical applications [18–20].

Recently, we reported the use of a boron nitride nanotube (BNNT) interlayer/film as an efficient heat dissipation layer which also improved mechanical and electrical performance of the resulting transparent heaters [21]. Martinez-Rubi *et al* have demonstrated successful dispersion of BNNTs using regiorandom poly (3-hexylthiophene-2,5-diyl) (rra-P3HT) to produce highly uniform and individualized BNNT dispersions that can be printed effectively [22]. This rra-P3HT and BNNT solution utilizes chloroform, a well-known harmful and carcinogenic solvent, however it provides the highest mole fraction solubility for P3HT [23]. Given the widespread use of rra-P3HT and BNNT solutions, it is of interest to investigate greener alternatives. Though chloroform solutions of rra-P3HT are effective, there are other polymers capable of interacting with and dispersing BNNT including polyvinyl alcohol, polyimide, polymethyl methacrylate, and polyvinyl butyral (PVB), all of which can be processed using green solvents such as ethanol and water [24, 25]. PVB in particular has demonstrated efficient compatibility with BN material while providing good processability [26–29].

In this study, we optimize the deposition of a PVB-modified BNNT using ethanol solvent to fabricate flexible microgrid heater architectures. We compare the solution properties and the printing processes to deposit the nanomaterial, as well as the resulting thin film properties to those obtained using P3HT and chloroform. We find that the use of PVB/ethanol provides a BNNT film with similar transmittance, resistance and mechanical properties compared to using P3HT/chloroform. When both polymer systems are utilized as dispersants to form BNNT interlayers between printed silver microgrid heaters and the substrate, they achieve similar heat-spreading properties, improve the temperature response, and reduce heat stress to the adjoining microgrid and underlying substrate in the same manner. We demonstrate a green solution for the deposition of active layers in emerging printed electronic applications that is easily adopted using standard coating methods.

## 2. Experimental methods

### 2.1. BNNT dispersion using $CHCl_3$ solvent

BNNT material was dispersed into two solutions using two different polymer and solvent combinations. Details regarding the synthesis and purification of the BNNT material can be found in works completed by Kim *et al* and Cho *et al* respectively [30, 31]. BNNT material was added to chloroform ($CHCl_3$) solvent and non-covalently functionalized with rra-P3HT (MW = 60–90 kDa) dissolved in $CHCl_3$ at an optimized 0.15 rra-P3HT:BNNT wt% ratio with the solution, and sonicated for 10 min between each addition of rra-P3HT [22, 32]. Excess rra-P3HT polymer was removed through vacuum filtration and the remaining rra-P3HT:BNNT solid content was redispersed into chloroform with a resulting BN concentration of 0.2 mg $ml^{-1}$. The rra-P3HT:BNNT solution was deposited onto clean polyethylene terephthalate (PET) substrates using an SC-150 slot-die applicator attached to an Automatic Research (GmBH) thin film coater and a Harvard Apparatus standard PHD 22/2000 syringe pump. Solvent was evaporated in ambient atmosphere for 30 s to achieve a calculated dry film thickness of 30 nm based on the coating speed, volumetric flowrate, coating width and solid content of the coating material [21].

### 2.2. Dispersion using alcohol solvent

BNNT material was added to ethanol (EtOH) followed by the incremental addition of PVB (MW = 40–70 kDa) dissolved in EtOH and subsequent sonication for 10 min to give an optimized 1:1 PVB:BNNT wt% ratio and final BN concentration of 0.2 mg $ml^{-1}$. The PVB:BNNT dispersion was spray-coated using an Iwata Eclipse HP-CS Gravity Feed Dual Action Airbrush and IS850 Smart Jet Compressor onto clean PET substrates placed on a heated platform set to 40 °C to assist in solvent evaporation. The substrate was coated back and forth until the entire substrate was covered to create one layer of PVB:BNNT on the substrate surface. This process was repeated following rotating the substrate 90° and repeating the deposition process to achieve multiple layers of PVB:BNNTs, resulting in samples coated with 4, 8, 12, and 16 layers of the PVB:BNNT. In addition, PVB without BNNT material was dissolved in EtOH with a final PVB concentration of 0.2 mg $ml^{-1}$ to mimic the solid content of the PVB:BNNT system and spray-coated onto clean PET substrates, totalling eight layers as described above.

### 2.3. Transparent heater fabrication

Silver molecular ink derived from silver neodecanoate was fabricated as described by Kell *et al* and screen-printed onto the dried BNNT-coated substrates as a grid pattern and processed through a combination of ultraviolet (UV) and thermal sintering techniques [33]. The grid pattern has a nominal line width of 50 $\mu$m, a pitch of 1300 $\mu$m and a total grid area of 1 × 1 inch. Further details regarding ink preparation as well as printing and processing details can be found in our previous work [21].

### 2.4. Characterization

After processing the ink, resistance measurements were taken using a handheld Fluke 115 Digital Multimeter by placing the probes onto the rectangular pads at either end of the printed grid to ensure proper connection and measuring across the pad for

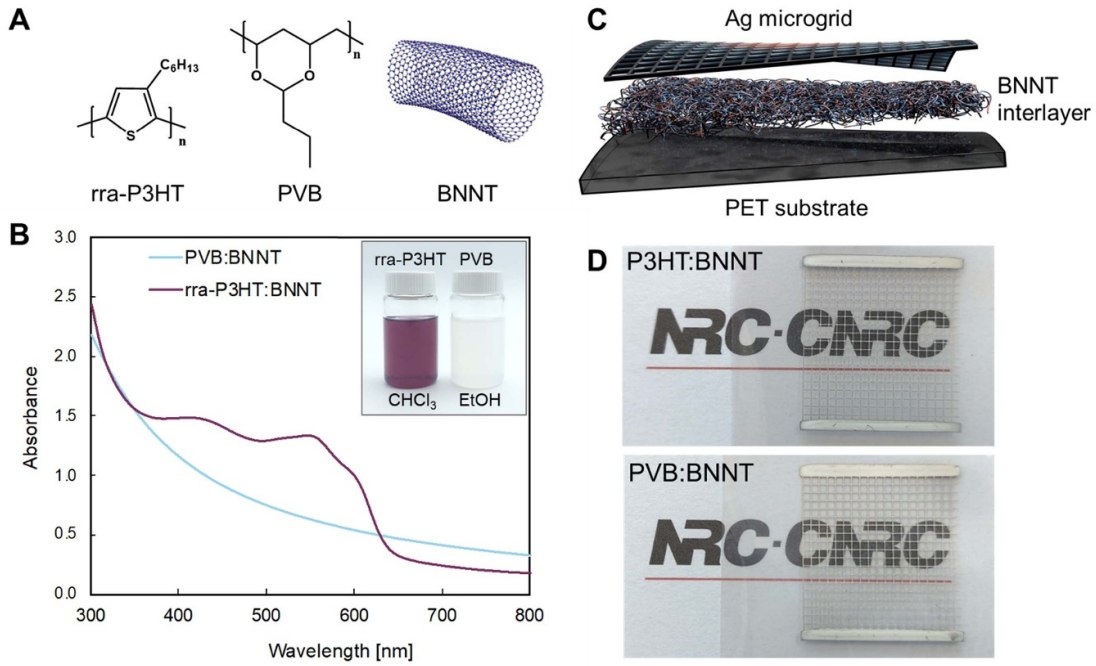


**Figure 1.** (A) Image of rra-P3HT and PVB polymer with boron nitride nanotube structure (B) absorbance spectra and corresponding images of rra-P3HT:BNNT stable dispersion in chloroform and PVB:BNNT dispersed in ethanol. Note: the BNNT-P3HT spectrum still contains excess P3HT ('bump' at ∼450 nm). After filtration to remove excess polymer, the corresponding signal at ∼450 nm is no longer present. (C) Structure of transparent heater architecture containing PET substrate, BNNT interlayer, and printed silver (Ag) microgrid. (D) Images of square grids printed on rra-P3HT:BNNT-coated PET and PVB:BNNT coated PET demonstrating transparency over logo.

a total of four measurements across the entire grid structure. Absorption spectra (figure 1(B)) and solid-state transmittance of the dried BNNT films on PET were taken using a Cary 5000 (UV–Vis) spectrometer, with optical transmittance (%T) measured to be 98.1% for the rra-P3HT:BNNT-coated PET and 97.2% for the PVB:BNNT-coated PET at a 500 nm wavelength (figure S1). A Biolin Scientific Attension Theta Optical Tensiometer was used to analyze surface energy of the BNNT-coated PET and accompanying Navitar camera and OneAttension software completed contact angle measurements of the films using water as the solvent. AFM topography imaging was performed on a MultiMode AFM with a NanoScope V controller (Bruker Nano Surfaces Division, Santa Barbara, CA, USA), in the Peak Force QNM mode. The peak force with which the tip taps the sample surface was always kept at the lowest stable imaging level of 200–400 pN. Silicon nitride ScanAsyst-Air AFM probes (Bruker AFM Probes, Camarillo, CA, USA) were used in all peak force feedback measurements. Scanning electron microscopy (SEM) was completed using a Hitachi SU5000 microscope and ultra-variable pressure detector with an accelerating voltage of 0.9–1.2 kV and 3.2 mm working distance and a ThermoFisher Scientific Apreo-2 SEM with an accelerating voltage of 0.5 kV and 3.1 mm working distance. Two-dimensional optical profilometry traces were measured with a cyberTECHNOLOGIES CT100 optical profilometer (cyberTECHNOLOGIES GmbH) and corresponding microscope images were taken with a Zeiss Axioscope 517/Vario upright microscope. Mechanical data was gathered using a tensile bend test with a mandrel of 10 mm radius as described by ASTM Standards, Designation: F 1683. The microgrid was bent and spun around the mandrel and then returned to its initial position so that the entirety of the grid was passed over the mandrel twice, which is considered one cycle in the testing regime. After 25 bending cycles, the resistances were measured in the same consistent areas along the microgrid so as to ensure accurate measurements and this change in resistance was plotted against each 25 cycle increments. Change in resistance was measured every 25 cycles at four consistent locations using the handheld Fluke 115 Digital Multimeter to ensure accurate measurements in the same manner described previously. To complete thermal performance testing, 3M copper tape with conductive adhesive was secured to the printed silver areas on either end of the grid and a voltage bias applied through a Global Specialties Model 1325 DC Power Supply. Continuous voltage was applied for 300 s and removed for 60 s, with corresponding thermal images and measured temperature response captured using a 5857 A TrueIR Thermal Imager by Keysight

Technologies every 7 s during the testing time. For the thermal cycling test, a customized 3D printed clip was produced that allowed for a copper electrode to remain in contact with the printed electrodes on the microgrid. The power supply was connected to the copper electrodes using alligator clips. A picture of this clip is presented in the supporting information in figure S2. Voltage was applied for 60 s and then removed for 60 s, representing one cycle, and then repeated for 18 cycles. The temperature response was captured with the same thermal camera used in the thermal performance testing.

## 3. Results and discussions

Chlorinated solvents are being banned in several manufacturing processes, and as such a shift in favour of more environmentally friendly solvents, such as alcohols, is growing in the manufacturing of printed electronics [34, 35]. BNNT inks are comprised of stable dispersions that use polymer-modified BNNTS dispersed in a solvent, and substitution of any of these components can lead to changes in their solution stabilities, processing qualities, as well as the resulting thin film properties. Therefore, when selecting a green solvent, the type of polymer and ratio of polymer to BNNT must be tuned to achieve optimal film properties. As detailed in the Experimental methods section, the PVB:BNNT system differs from the rra-P3HT:BNNT system in two key ways. First, the rra-P3HT can stabilize BNNTs at a 0.15:1 wt% ratio while the PVB requires a 1:1 wt% ratio to reach a similar level of dispersion stability, due to the different type of interactions involved between the polymer and the BNNTs. Second, the significant difference in boiling points of the two solvents impacted how the dispersion could be deposited to achieve high film uniformity. At 25 °C, the chloroform of the rra-P3HT:BNNT system has a vapour pressure roughly 2.5 times greater than ethanol present in the PVB:BNNT system (17.8 kPa vs. 7.9 kPa) with almost half the viscosity (0.54 mPa·s vs. 1.1 mPa·s) [36–38]. In our previous study, we demonstrated that slot-die coating deposition methods achieved uniform films of the rra-P3HT:BNNT [21]. However, upon deposition of the PVB:BNNT system using the same slot-die coating procedure, the slow evaporation time of the ethanol solvent resulted in the solution pooling on the substrate surface and precipitation of the BNNTs, leading to poor dried film uniformity. Attempts to optimize the slot-die coating, including wet film thickness, blade height, blade speed, and depositing temperature resulted in small areas of uniform film across a larger sample area, however large area film consistency was unattainable. Spray-coating was adopted to deposit the PVB:BNNT system by taking advantage of the atomized output from the spray gun on a substrate heated at 40 °C, leading to uniform thin films.

Varying layer depositions of 4, 8, 12, and 16 layers of the spray-coated PVB:BNNT dispersion were investigated to optimize conductive and thermal performance of the grids. A sufficient amount of layers is essential in determining a dense-enough network to take advantage of the heat spreading abilities of the BNNTs without disturbing the print quality or accumulating material waste. Upon printing of the microgrid onto the PVB:BNNT-coated substrates, those printed on 4 and 8 layers achieved very similar resistance values. However, those printed on 12 and 16 layers experienced a reduced print quality when the wet ink was deposited onto the substrate, and disconnects were visible within the grid mesh area. When measuring resistance post-processing, it was determined that the microgrid printed on 16 layers was non-conductive as a result of the poor printability and therefore could not be considered viable. Demonstration of the 4, 8 and 12 layer PVB:BNNT microgrids are shown in later experiments to confirm which architecture provides the most optimal conductive and thermal performance.

SEM imaging was conducted on the rra-P3HT:BNNT and PVB:BNNT thin films. As shown in figures 2(A) and (B), the BNNTs with rra-P3HT were deposited across the film, and although evidence of tube bundling is apparent, there is a clear uniform and dense tube network across the entire substrate. The films also contain particulates of BN material however these components do not prevent the BNNTs from forming a uniform network. In figure 2(C), atomic force microscopy (AFM) height image of the rra-P3HT:BNNT film is presented and provides insight into the average roughness ($R_a$) of the film surface, measuring 20 nm. In figures 2(D) and (E), SEM images reveal that the eight-layer PVB:BNNT system deposited using spray coating also formed a sufficiently dense network of BNNTs on the substrate surface. The PVB:BNNT films appear denser than the rra-P3HT:BNNT, likely due to the greater polymer concentration in the solution or the multiple layers which were deposited. AFM height image of the eight-layer PVB:BNNT film is presented in figure 2(F), which measures the $R_a$ of the film's surface to be 20 nm. To further characterize the thin films using AFM techniques, $R_a$ and the root-mean-square roughness ($R_q$) were accumulated across a distribution of 20 different areas of the rra-P3HT:BNNT and PVB:BNNT systems, respectively. The rra-P3HT:BNNT film exhibits a relatively even $R_a$ across the sample size ($n = 20$) between 18–28 nm and an $R_q$ range of 26–38 nm. In comparison, the PVB:BNNT system reveals a greater variability for both the $R_a$ and $R_q$ values, ranging from 13–35 nm and 19–53 nm, respectively. Additional AFM images of both the rra-P3HT:BNNT and PVB:BNNT films can be found in figure S3 along with corresponding peak force error imaging to provide further insight into the variability of the films' surface morphology.

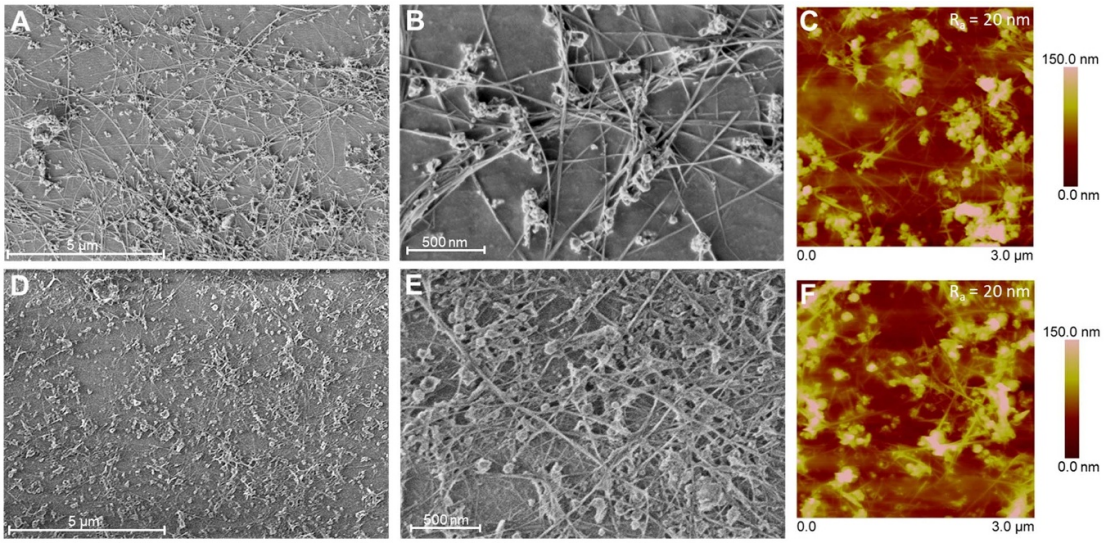


**Figure 2.** (A) SEM images of rra-P3HT:BNNT deposited using slot-die coating methods with (B) corresponding high magnification imaging and (C) representative AFM height image of the rra-P3HT:BNNT system. (D) SEM images of PVB:BNNT deposited using spray coating methods with (E) corresponding high magnification imaging of the PVB:BNNT system and (F) representative AFM height image of the PVB:BNNT system.

Figure S4 and table S1 provide further details regarding the plotted distribution of the $R_a$ and $R_q$ and the calculated mean, standard deviation, and median values of the rra-P3HT:BNNT and PVB:BNNT films.

The greater variability of the PVB:BNNT films is likely due to the increased polymer content that can accumulate on the surface of the samples or between layers of nanotubes and BN material resulting in a more uneven film. We expect greater variability in the surface roughness of the films deposited by atomized spray coating in comparison to slot die coating because it offers less control over the orientation of the BNNT resulting in some deposition of the nanomaterial perpendicular to the substrate surface. However, the surface roughness remains well below the height of the silver microgrids printed onto the BNNT interlayer, and we do not believe the differences in surface roughness are causing any changes in performance as will be highlighted below.

Fabrication of transparent heaters is accomplished by depositing silver traces directly onto the BNNT-coated substrate [21]. A silver molecular ink was deposited as a square grid shape using screen-printing methods on the BNNT-coated PET, where each square grid pattern measured a nominal line width of 50 $\mu$m, a nominal pitch of 1300 $\mu$m with a total grid area of 1 in [2]. The printed grid samples then underwent a consecutive UVA treatment and thermal sintering in order to initiate and complete the reduction from $Ag^+$ to $Ag^0$ to convert the ink into silver traces [39]. Resistance measurements conducted resulted in an averaged resistance of 1.89 $\pm$ 0.19 $\Omega$ across nine samples printed on rra-P3HT:BNNT-coated PET and an averaged resistance of 2.22 $\pm$ 0.20 $\Omega$ across ten samples printed on PVB:BNNT-coated PET. Optical 2D profilometry and microscope imaging of the traces are presented in figure 3 to investigate trace morphology. The surface profile of the rra-P3HT:BNNT system (figure 3(A)), depicts varying peaks and valleys throughout the trace, with an average height of 0.62 $\mu$m, a maximum measured height of 1.29 $\mu$m an $R_q$ of 0.17 $\mu$m. Corresponding microscope images of the traces printed on rra-P3HT:BNNT-coated PET is presented in figure 3(B), and confirms the dense randomized networks of silver veins throughout the bulk of the trace that is directly responsible for the peaks and valleys measured in figure 3(A). Surface energy analysis was conducted on the BNNT film to provide insight into the interactions of the silver ink with the different surfaces during printing. As shown in figure 3(B) inset, a 3 $\mu$L water drop deposited on the rra-P3HT:BNNT film results in a contact angle of 92.6° which is consistent with previous reports [21]. In comparison, the cross-sectional height profile of the trace printed on PVB:BNNT-coated PET in figure 3(C) exhibits three distinct peaks on the trace surface at either end and in the middle of the trace, resulting in an average height measurement of 0.49 $\mu$m, a maximum height of 1.14 $\mu$m and an $R_q$ of 0.10 $\mu$m. When analyzing the microscope image of the PVB:BNNT system in figure 3(D), the three peaks depicted in the surface height profiles are apparent by the more concentrated silver veins that formed during processing. Because the silver grids printed on PVB:BNNT are not as thick as those printed on the rra-P3HT:BNNT, that alongside the different surface morphology of the trace on

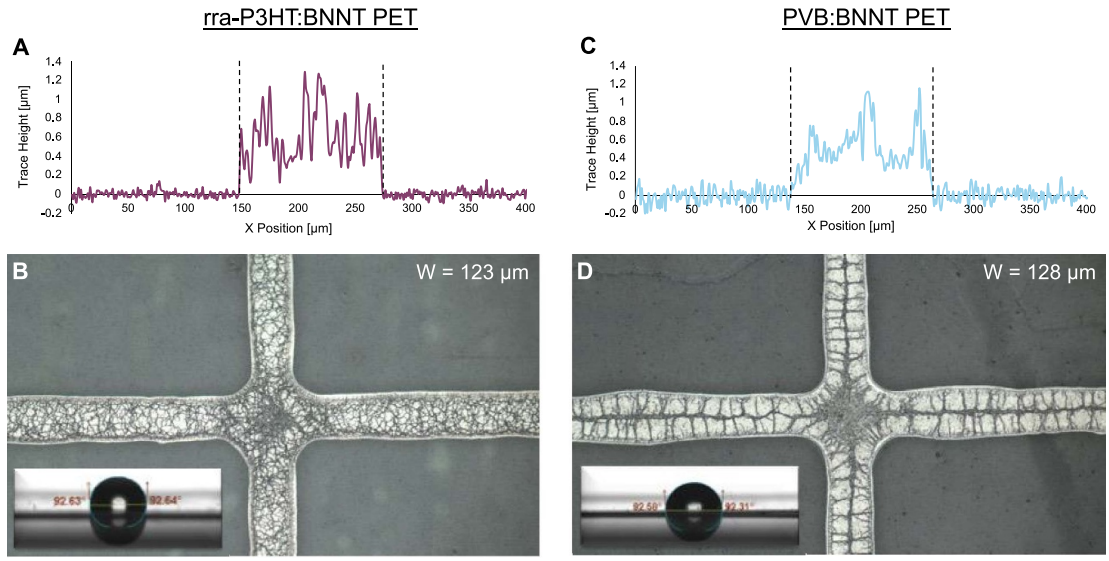


**Figure 3.** Optical 2D profilometry measurement of the Ag microgrid sample printed on (A) rra-P3HT:BNNT-coated PET with (B) corresponding microscope images of the traces with contact angle image inset and optical 2D profilometry measurements of the Ag microgrid sample printed on (C) PVB:BNNT-coated PET substrates with (D) corresponding microscope image of the trace with contact angle image inset.

PVB:BNNT likely leads to less silver metal present and subsequently the slight difference in electrical performance. The contact angle measurement for the PVB:BNNT system in figure 3(D) inset also presents a contact angle of 92.6°, indicating that the increased surface roughness of the PVB:BNNT film as presented in figure 2 does not affect surface hydrophobicity, further evident by the similar measured trace widths (W) of 123 $\mu$m and 128 $\mu$m in figures 2(B) and 2(D) respectively.

The profilometry data also provides insight into the measured height of the polymer:BNNT coating from the surface of the PET substrate, with a maximum measured height of 105 nm for the rra-P3HT:BNNT film and 191 nm for the PVB:BNNT film which is significantly higher relative to the rra-P3HT:BNNT system. Slight difference in the manner that the silver salt converts to silver metal may be expected given that the thermal properties of the underlying BNNT films differ due to differences in the polymer and polymer:BNNT, as shown in the trace images in figure 3.

The robustness of the printed microgrid traces on rra-P3HT:BNNT and PVB:BNNT were characterized by subjecting the microgrids to a series of tensile bending cycles, as shown in figure 4(A). Typically, a 10% increase in resistance is considered the maximum allowable increase before the samples are considered to have failed. Within the first 150 bending cycles, the microgrid printed on PVB:BNNT-coated PET is able to maintain a smaller change in resistance when subjected to the tensile bending tests compared to the microgrid printed on rra-P3HT:BNNT. At roughly 150 cycles both the PVB:BNNT and rra-P3HT:BNNT have a % change in resistance of over 10%, demonstrating both films exhibit near identical response to mechanical deformation. In addition to investigating mechanical robustness of the BNNT interlayers, the thermal response of the microgrid printed on each interlayer must also be tested. It has been shown that the inclusion of a BNNT interlayer between the plastic substrate and printed feature can improve the Joule heating effect through electrical sintering, leading to an increase in heat output from the microgrid [21, 40]. However, substitution of the polymeric materials, differences in polymer solid content, and the morphology of the films may change the thermal response of the grids. The thermal performance of microgrids printed on 0, 4, 8 and 12 layers ($R$ = 2.03, 2.50, 2.10, 2.05 Ω respectively) of PVB:BNNT was investigated to determine whether a sufficient network of BNNTs were deposited to take advantage of the thermal conductivity of the BNNT network and initiate their heat spreading abilities. Upon applied voltage of 2.5 V, the eight-layer sample provided a clear improvement in uniform Joule heating across the grid area, whereas the 4- and 12-layer samples showed non-uniform thermal response with evident hot-spots throughout the grid area, as shown in figure S5. As a result, the thermal performance of the silver microgrid printed on PVB-coated PET, rra-P3HT:BNNT-coated PET, and eight-layer PVB:BNNT-coated PET were further characterized. The measured resistances of the grids were 1.83 Ω, 2.00 Ω, and 2.05 Ω respectively. It is important to note that grids with similar base resistances were compared to ensure that observed differences were a result of the change in material selection. The grids were subjected to applied voltages of 1.0, 1.5, 2.0 and 2.5 V consecutively, with each voltage applied for 300 s with

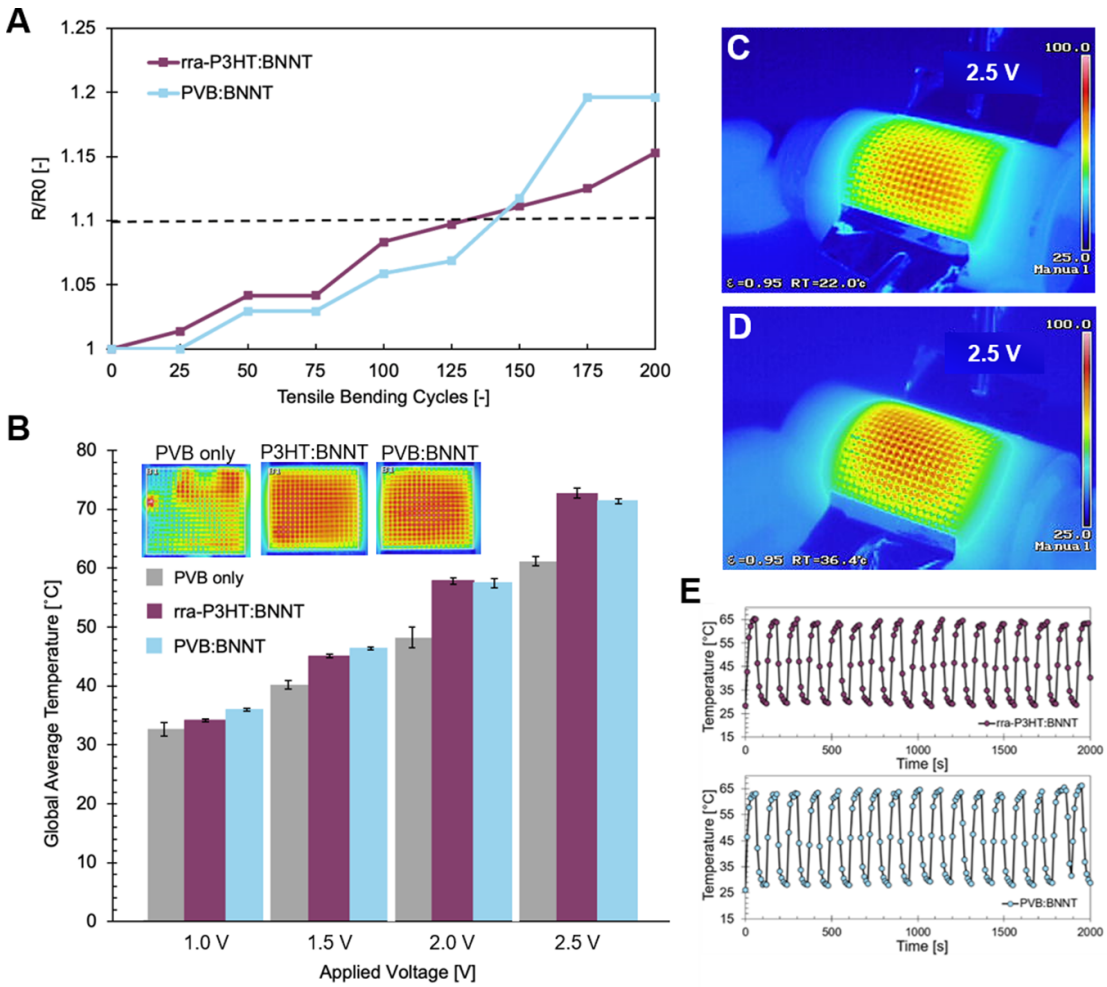


**Figure 4.** (A) Comparison of change in resistance of the Ag microgrids printed on rra-P3HT:BNNT-coated PET and PVB:BNNT-coated PET over 200 total tensile bending cycles. (B) Averaged global temperature response of the Ag microgrid printed on PVB film, rra-P3HT:BNNT and PVB:BNNT systems at applied voltages of 1.0, 1.5, 2.0 and 2.5 V with inset images at 2.5 V at $t = 160$ s (C) steady-state thermal response of the Ag microgrid printed on rra-P3HT:BNNT and (D) PVB:BNNT at $t = 125$ s upon applied 2.5 V flexed around a scintillation vial at $t = 280$ s and (E) thermal cycling response of Ag microgrids printed on rra-P3HT:BNNT and PVB:BNNT films respectively at an applied voltage of 2.3 V.

measurements taken every 7 s until 60 s after the voltage is removed. The averaged steady-state temperatures collected for 240 s at each applied voltage are presented in figure 4(B), excluding the measurements of the temperature ramp-up and cool down post testing.

As shown in figure 4(B), the PVB:BNNT system has a near identical measured temperature response to that of the rra-P3HT:BNNT system at each applied voltage, indicating that the PVB polymer complex is able to support the BNNT material and allow it to dissipate heat laterally across the grid area and improve the overall Joule heating response. In comparison, the microgrid printed onto the PVB-coated substrate shows an uneven temperature distribution and hot spot formation throughout the feature, indicating that the BNNTs are integral in spreading heat across the entire feature area. Characteristic thermal images of the steady state temperature response of the three microgrids at each applied voltage are provided in figures S6–S8. Both samples printed on BNNT-coated PET demonstrate an even and uniform distribution of heat across the entire grid area, with sufficient heat spreading on part from the BNNT interlayer as well as the high-quality trace morphology from both samples. Furthermore, the grids were also tested by wrapping and securing around a vial with a diameter of 2.8 cm, and the temperature response measured in the same manner as the flat thermal characterization. There is no hot spot formation or delamination as seen in the thermal imaging in figures 4(C) and (D), indicating that both the rra-P3HT:BNNT and PVB:BNNT interlayers continue to assist in spreading heat laterally across the microgrid area to produce an even heat distribution even when flexed. Finally, to explore the operational stability of the polymer:BNNT interlayers, thermal cycling tests were completed on the 50/1300 microgrid printed on both rra-P3HT:BNNT and PVB:BNNT systems. As presented in figure 4(E), a voltage of 2.3 V was applied

for 60 s and then removed for 60 s over a consistent 36 min testing period, with measurements of the global average temperature response across the entire grid area taken every 10 s. At near identical resistances of 1.50 and 1.56 Ω for the Ag microgrids printed on rra-P3HT:BNNT and PVB:BNNT interlayers respectively, both polymer:BNNT systems provide a sufficient and reliable platform to withstand the thermal cycling, achieving nearly identical temperature profiles with little degradation over time. This further demonstrates the ability for the PVB:BNNT to form a similar network to rra-P3HT:BNNT which can provide significant improvements in thermal performance in transparent thermal heaters.

## 4. Conclusion

In this study we report the use of PVB and ethanol as a green alternative to using P3HT and chloroform for the printing of BNNT thin films. We determined that similar BNNT films, tube network formation, surface energy, and transparency can be obtained when optimizing the polymer to BNNT ratio and when using spray coating deposition techniques. A more variable surface roughness of the PVB:BNNT film did not affect the deposition of the molecular ink, and the microgrid transparent heater printed on PVB:BNNT-coated PET achieved similar resistance values ($2.22 \pm 0.20$ Ω) to that of the microgrid printed on rra-P3HT:BNNT-coated PET ($1.89 \pm 0.19$ Ω) as well as a lower RMS roughness value of the trace surface post-processing. Furthermore, the PVB:BNNT-coated PET produced similar responses to tensile cyclic deformation, indicating that both BNNT interlayers can alleviate the mechanical stress imparted on the silver grid traces. Finally, the rra-P3HT:BNNT and PVB:BNNT systems exhibit near identical averaged temperature responses of $72.7 \pm 0.80$ °C and $71.4 \pm 0.43$ °C respectively upon applied voltage of 2.5 V. Therefore, this study demonstrates the ability for the PVB:BNNT system to form a sufficient tube network necessary to achieve similar mechanical and thermal performance metrics as the previous rra-P3HT:BNNT system while being processed using green solvents.

## Data availability statement

All data that support the findings of this study are included within the article (and any supplementary files).

## Acknowledgments

This work was supported by the NSERC Green Electronics Network (GreEN) (Grant No. NETGP 508526-17). We thank Mark Plunkett, Dean Ruth, Keun Su Kim, and Benoit Simard for the synthesis and purification of the BNNTs utilized in this study. We also thank Nic Milliken for the design and fabrication of the 3D-printed clips to test thermal cycling.

## Author contributions

K W, C P, Y R-M and B L conceived the idea and designed the project.; K W led the fabrication and surface characterization and S Z led the atomic force microscopy characterization; K W led the electro-optical characterization, and mechanical and thermal studies, with assistance from A K in thermal response testing.; K W and B L wrote the text and designed the figures.; C P and B L supervised the research conducted.; All authors commented on the manuscript.

## Conflict of interest

The authors declare no competing financial or non-financial interests.

## ORCID iD

Benoît H Lessard https://orcid.org/0000-0002-9863-7039

## References

[1] Baumbauer C L, Anderson M G, Ting J, Sreekumar A, Rabaey J M, Arias A C and Thielens A 2020 Printed, flexible, compact UHF-RFID sensor tags enabled by hybrid electronics *Sci. Rep.* **10** 16543
[2] Li Z, Khuje S, Chivate A, Huang Y, Hu Y, An L, Shao Z, Wang J, Chang S and Ren S 2020 Printable copper sensor electronics for high temperature *ACS Appl. Electron. Mater.* **2** 1867–73
[3] Lo L, Shi H, Wan H, Xu Z, Tan X and Wang C 2020 Inkjet-printed soft resistive pressure sensor patch for wearable electronics applications *Adv. Mater. Technol.* **5** 1900717
[4] Ma L-Y and Soin N 2022 Recent progress in printed physical sensing electronics for wearable health-monitoring devices: a review *IEEE Sens. J.* **22** 3844–59
[5] Machiels J *et al* 2021 Screen printed antennas on fiber-based substrates for sustainable HF RFID assisted E-fulfilment smart packaging *Materials* **14** 5500
[6] Correia V, Mitra K Y, Castro H, Rocha J G, Sowade E, Baumann R R and Lanceros-Mendez S 2018 Design and fabrication of multilayer inkjet-printed passive components for printed electronics circuit development *J. Manuf. Process.* **31** 364–71
[7] Chang J S, Facchetti A F and Reuss R 2017 A circuits and systems perspective of organic/printed electronics: review, challenges, and contemporary and emerging design approaches *IEEE J. Emerg. Sel. Top. Circuits Syst.* **7** 7–26
[8] Savva A *et al* 2019 Solvent engineering for high-performance N-type organic electrochemical transistors *Adv. Electron. Mater.* **5** 1900249
[9] Byrne F P, Jin S, Paggiola G, Petchey T H M, Clark J H, Farmer T J, Hunt A J, Robert Mcelroy C and Sherwood J 2016 Tools and techniques for solvent selection: green solvent selection guides *Sustain. Chem. Process.* **4** 7
[10] Campana F, Kim C, Marrocchi A and Vaccaro L 2020 Green solvent-processed organic electronic devices *J. Mater. Chem. C* **8** 15027–47
[11] Lee J, Park S A, Ryu S U, Chung D, Park T and Son S Y 2020 Green-solvent-processable organic semiconductors and

future directions for advanced organic electronics *J. Mater. Chem.* A **8** 21455–73
[12] Larsen C, Lundberg P, Tang S, Ràfols-Ribé J, Sandström A, Mattias Lindh E, Wang J and Edman L 2021 A tool for identifying green solvents for printed electronics *Nat. Commun.* **12** 4510
[13] McDowell C and Bazan G C 2017 Organic solar cells processed from green solvents *Curr. Opin. Green Sustain. Chem.* **5** 49–54
[14] Kim D and Nunes S P 2021 Green solvents for membrane manufacture: recent trends and perspectives *Curr. Opin. Green Sustain. Chem.* **28** 100427
[15] Chen Y, Zhuang X, Goldfine E A, Dravid V P, Bedzyk M J, Huang W, Facchetti A and Marks T J 2020 Printable organic-inorganic nanoscale multilayer gate dielectrics for thin-film transistors enabled by a polymeric organic interlayer *Adv. Funct. Mater.* **30** 2005069
[16] Sekine T, Ikeda H, Kosakai A, Fukuda K, Kumaki D and Tokito S 2014 Improvement of mechanical durability on organic TFT with printed electrodes prepared from nanoparticle ink *Appl. Surf. Sci.* **294** 20–23
[17] Domínguez M A and Sosa-Sánchez J L 2020 Copper phthalocyanine buffer interlayer film incorporated in paper substrates for printed circuit boards and dielectric applications in flexible electronics *Solid State Electron.* **172** 107898
[18] Yang J, Zi D, Zhu X, Li H, Li Z, Sun L, Zhang G, Wang F, Peng Z and Lan H 2022 Printed flexible transparent electrodes for harsh environments *Adv. Mater. Technol.* **7** 2101087
[19] Li Z, Chang S, Khuje S and Ren S 2021 Recent advancement of emerging nano copper-based printable flexible hybrid electronics *ACS Nano* **15** 6211–32
[20] Chen X, Yin Y, Yuan W, Nie S, Lin Y, Guo W, Su W, Li Y, Yang K and Cui Z 2021 Transparent thermotherapeutic skin patch based on highly conductive and stretchable copper mesh heater *Adv. Electron. Mater.* **7** 2100611
[21] Wagner K, Kell A J, Martinez-Rubi Y, Paquet C and Lessard B H 2022 Engineering silver microgrids with a boron nitride nanotube interlayer for highly conductive and flexible transparent heaters *Adv. Mater. Technol.* **7** 2200037
[22] Martinez-Rubi Y, Jakubek Z J, Jakubinek M B, Kim K S, Cheng F, Couillard M, Kingston C and Simard B 2015 Self-assembly and visualization of poly (3-hexyl-thiophene) chain alignment along boron nitride nanotubes *J. Phys. Chem.* C **119** 26605–10
[23] Roesing M, Howell J and Boucher D 2017 Solubility characteristics of poly (3-hexylthiophene) *J. Polym. Sci.* B **55** 1075–87
[24] Joy J, George E, Haritha P, Thomas S and Anas S 2020 An overview of boron nitride based polymer nanocomposites *J. Polym. Sci.* **58** 3115–41
[25] Sharma S, Setia P, Chandra R and Thakur N 2020 Experimental and molecular dynamics study of boron nitride nanotube-reinforced polymethyl methacrylate composites *J. Compos. Mater.* **54** 3–11
[26] Zhi C, Bando Y, Terao T, Tang C, Kuwahara H and Golberg D 2009 Towards thermoconductive, electrically insulating polymeric composites with boron nitride nanotubes as fillers *Adv. Funct. Mater.* **19** 1857–62
[27] Wang J, Wang N, Liu M, Ge C, Hou B, Liu G, Sun W, Hu Y and Ning Y 2022 Hexagonal boron nitride/poly (vinyl butyral) composite coatings for corrosion protection of copper *J. Mater. Sci. Technol.* **96** 103–12
[28] Ahn H J, Eoh Y J, Park S D and Kim E S 2014 Thermal conductivity of polymer composites with oriented boron nitride *Thermochim. Acta* **590** 138–44
[29] Wang Z, Liu J, Cheng Y, Chen S, Yang M, Huang J, Wang H, Wu G and Wu H 2018 Alignment of boron nitride nanofibers in epoxy composite films for thermal conductivity and dielectric breakdown strength improvement *Nanomaterials* **8** 242
[30] Kim K S, Kingston C T, Hrdina A, Jakubinek M B, Guan J, Plunkett M and Simard B 2014 Hydrogen-catalyzed, pilot-scale production of small-diameter boron nitride nanotubes and their macroscopic assemblies *ACS Nano* **8** 6211–20
[31] Cho H *et al* 2020 Scalable gas-phase purification of boron nitride nanotubes by selective chlorine etching *Chem. Mater.* **32** 3911–21
[32] Martinez Rubi Y, Jakubek Z J, Chen M, Zou S and Simard B 2019 Quality assessment of bulk boron nitride nanotubes for advancing research, commercial, and industrial applications *ACS Appl. Nano Mater.* **2** 2054–63
[33] Kell A J *et al* 2017 Versatile molecular silver ink platform for printed flexible electronics *ACS Appl. Mater. Interfaces* **9** 17226–37
[34] Medina-Gonzalez Y, Camy S and Condoret J-S 2014 $ScCO_2$/green solvents: biphasic promising systems for cleaner chemicals manufacturing *ACS Sustain. Chem. Eng.* **2** 2623–36
[35] Heidari S M and Anctil A 2020 Identifying alternative solvents for $C_{60}$ manufacturing using singular and combined toxicity assessments *J. Hazards Mater.* **393** 122337
[36] Oracz P and Kolasi G 1987 Total vapour pressure measurements for binary mixtures of methanol, ethanol, 1-propanol and 1-butanol with benzene, toluene and p-xylene at 313.15 K *Fluid Phase Equilib.* **35** 253–78
[37] Oswal S and Rathnam M V 1984 Viscosity data of binary mixtures: ethyl acetate + cyclohexane, + benzene, + toluene, + ethylbenzene + carbon tetrachloride, and + chloroform at 303.15 K *Can. J. Chem.* **62** 2851–3
[38] Gonçalves F A M M, Trindade A R, Costa C S M F, Bernardo J C S, Johnson I, Fonseca I M A and Ferreira A G M P V T 2010 Viscosity, and surface tension of ethanol: new measurements and literature data evaluation *J. Chem. Thermodyn.* **42** 1039–49
[39] Liu X *et al* 2021 UV-sinterable silver oxalate-based molecular inks and their application for in-mold electronics *Adv. Electron. Mater.* **7** 2100194
[40] Wagner K, Paquet C, Martinez-Rubi Y, Genest M, Guan J, Sampson K L, Kim K S, Kell A J, Malenfant P R L and Lessard B H 2021 Boron nitride nanotube coatings for thermal management of printed silver inks on temperature sensitive substrates *Adv. Electron. Mater.* **7** 2001035